Towards a predictive understanding of direct ink writing of graphene-based inks

Applied Materials Today 36 (2024) 102014

Contents lists available at ScienceDirect

Applied Materials Today

journal homepage: www.elsevier.com/locate/apmt

Towards a predictive understanding of direct ink writing of graphene-based inks

Laura S. van Hazendonk [a,b], Coen F. Vonk [a], Wilko van Grondelle [a], Niels H. Vonk [c], Heiner Friedrich [a,b,*]

[a] Laboratory of Physical Chemistry and Center for Multiscale Electron Microscopy, Department of Chemical Engineering and Chemistry, Eindhoven University of Technology, PO box 513, 5600 MB Eindhoven, the Netherlands

[b] Institute for Complex Molecular Systems, Department of Chemical Engineering and Chemistry, Eindhoven University of Technology, PO box 513, 5600 MB Eindhoven, the Netherlands

[c] Department of Mechanical Engineering, Eindhoven University of Technology, PO box 513, 5600 MB Eindhoven, the Netherlands

ARTICLE INFO

Keywords:
Graphene
Direct ink writing
Printed electronics
Wearables
Stretchable conductors
Design of experiments

ABSTRACT

Direct ink writing (DIW) presents a flexible and resource-efficient approach towards the prototyping of functional materials and devices with complex shapes. Printed functional materials for electronic devices depend on conductive fillers such as graphene nanoplatelets (GNPs), which are increasingly popular in printed electronics and energy materials thanks to their low cost, non-toxicity and high specific surface area. However, non-spherical colloids with large filler-to-nozzle size ratios like GNPs present a challenge for high-resolution DIW due to risk of nozzle clogging. As DIW of platelet-based inks is gaining traction in several fields, the feasibility of high-resolution DIW of platelet-based inks is demonstrated here on the example of GNPs (< 50 μm). A workflow for the combined optimization of ink rheology and printing process parameters was developed to gain a predictive understanding of filament quality and morphology. Using two inks and two nozzle diameters per ink, filaments ranging from <100 – 1200 μm in width and 30 – 300 μm in height were produced, with conductivities suitable for application in sensors or electrodes. The derived predictive models were successfully deployed to predict filament dimensions and to achieve excellent print quality even for fine sub-nozzle size structures with very high filler-to-nozzle size ratios within only one iteration of the workflow. With this study, we advocate for the integrated development of materials for processes and processes for materials. This study will benefit high-resolution rapid prototyping of a large class of functional materials for wearable electronics, sensors, RF passives, energy materials and tissue engineering.

1. Introduction

Graphene-based printed conductors are increasingly popular thanks to their low cost, biocompatibility, high specific surface area and absorbance of radiation [1–3]. This makes these conductors particularly suitable for application in wearable electronics [4–6], sensors [7,6,8–10], energy materials [3,11], and passive radio frequency (RF) hardware [12,13]. Such functional materials require hierarchical structuring, which could be achieved by combining top-down and bottom-up structuring approaches.

Direct ink writing (DIW) presents a flexible and resource-efficient approach towards the prototyping of complex functional materials as it enables unprecedented control over ink deposition, and even enables three-dimensional (3D) and potentially also conformal printing [14–17,3,18]. In DIW, also termed robocasting, ink is extruded from a robotic dispensing device which is controlled by computer code (G-code) [18]. Extrusion is controlled by either air pressure, an electric piston or screw injection [18]. The computer-aided design in combination with 3D patterning and compatibility with many substrates provides the user with huge design freedom and flexibility, which makes the technique ideal for lab-scale manufacturing of intricate parts or prototyping of colloidal suspensions [14,18]. DIW covers a large design space thanks to nozzle diameters ranging from sub-100 micron up to beyond 1 mm [18]. This design space is much larger than that of other common additive manufacturing techniques such as inkjet printing, and it presents a relevant design space for graphene nanoplatelets (GNPs). Within this 0.1–1 mm range, large GNPs maintain their functional properties like conductivity, while the resulting prints are of high resolution. Suitable inks are needed to cover this design space, with properties matching the selected nozzle diameter and the desired functionality of the resulting prints. Hence, there is a need for the integrated development of materials for processes and processes for materials.

* Corresponding author at: Laboratory of Physical Chemistry and Center for Multiscale Electron Microscopy, Department of Chemical Engineering and Chemistry, Eindhoven University of Technology, PO box 513, 5600 MB Eindhoven, the Netherlands.
E-mail address: h.friedrich@tue.nl (H. Friedrich).

https://doi.org/10.1016/j.apmt.2023.102014
Received 30 August 2023; Received in revised form 1 November 2023; Accepted 5 December 2023
Available online 14 December 2023

Printing of functional materials requires a high level of control over the deposition in terms of filament height, base width and full-width-at-half-maximum (FWHM), for the morphology affects the material's functional properties such as the conductivity [6,19]. Conventionally, most DIW processes rely on trial-and-error-based process optimization for a specific ink, while a predictive understanding of the printing process is lacking [20]. Functional inks made from non-spherical colloids like GNPs present a particular challenge for high resolution printing with small nozzles, where nozzle clogging may occur [21–23]. Especially fillers with diameters exceeding 1/100th or even 1/150th of the nozzle diameter, such as concentrated GNP suspensions, are termed challenging for printing [24,23,21], while large GNPs are desirable to achieve good conductivity. Platelet size thus presents a trade-off between print resolution and conductivity. Joint optimization of the ink and printing conditions is therefore required for a controlled deposition morphology of printed functional materials with controlled filament morphology and conductivity. For inks containing large graphene nanoplatelets as conductive fillers, a systematic investigation on the effect of DIW print parameters and ink properties on the reachable design space like print morphologies and conductivities towards a predictive understanding of the print properties, is missing.

In this study, we aim to fill this knowledge gap by demonstrating the feasibility of direct ink writing of platelet-based inks on the example of GNPs with the end goal of enabling rapid prototyping of a large class of functional materials for wearable electronics, sensors, electrodes for energy materials and RF passives. The specific focus of this work is on the combined optimization of ink rheology and printing process parameters to determine the accessible design space for ink and nozzle combinations and to develop a predictive understanding of deposited filament morphology. We aim to utilize the DIW-enabled design space ranging from circa 100 μm up to 1 mm in combination with inks containing polydisperse GNPs of approximately 1–50 μm in diameter, which requires both ink and printing process to be optimized and matched. To this end we implemented an efficient and general workflow consisting of ink design based on the printer-imposed boundary conditions, ink characterization, finding the overlap between the design spaces of the printer and the ink, and finally print settings optimization using smart sampling with Design of Experiments (DoE) and efficient test structures. This resulted in the successful printing of fine lines with FWHM down to 104 μm through a nozzle with an upper filler-to-nozzle ratio of approximately 1/7. Our proposed methodology to find optimum print settings can be adjusted to any shear-thinning ink. With this study, we contribute to the field of hierarchically structured materials for energy and healthcare applications highlighting the importance of integrated development of materials for processes and processes for materials.

2. Experimental section

2.1. Ink preparation

Two inks were prepared according to a previously described procedure [4] using a thermoplastic polyurethane (TPU) binder and two different graphene nanoplatelet (GNP) sources. The first ink was made from thermally expanded graphite (TEG), prepared as described elsewhere [4,25]. The second ink was made from commercial GNP with a diameter of roughly 5 μm, supplied by XG-sciences (grade M5). Each ink was made with a GNP-to-binder ratio of 1:3, for this was previously found to present the optimum in terms of ink rheology, print quality and conductivity [4,26]. The two inks are further referred to as TEG-ink and M5-ink, respectively.

For TEG-ink preparation, ethyl acetate (BioSolve Chimie) and isopropyl alcohol (VWR Chemicals) were mixed in a 4:1 (v/v) ratio in a 1 L glass cylinder. To 500 mL of this solvent blend, 0.75 g ethyl cellulose (EC) was added, followed by mixing for 5 min at 3000 RPM with an Ystral X40/38 high-shear mixer equipped with a stator with an internal diameter of 35 mm and a 25 mm rotor. 5 g of TEG was added to the ethyl cellulose solution, followed by high-shear exfoliation for 60 min at 7000 RPM while cooling with ice-water. Afterwards, the contents of the cylinder were left to settle for 60 min to remove the largest, non-exfoliated graphitic particles. The supernatant was decanted into a clean 1 L cylinder. Subsequently, 22.5 g of NeoRez U-431 binder and 45 g of glycol ethers were added, followed by 5 min of mixing at 3000 RPM after addition of each chemical. The mixture was decanted into a round-bottom flask for solvent exchange in a rotary evaporator (1 h at 200 mbar).

For the M5-ink, a 2 L glass cylinder was filled with 1 L of ethyl acetate and isopropyl alcohol (4:1 v/v). Subsequently, 1.65 g EC was incorporated by mixing for 5 min at 3000 rpm, after which 12 g of M5 GNP was added and mixed for 5 min at 5000 rpm. Next, the mixing speed was reduced to 3000 rpm, followed by incorporation of 90 g NeoRez U-431 binder (Covestro) and 60 g glycol ethers (dowanol PnB, Sigma-Aldrich). After addition of each component, the ink was mixed for 5 min at 3000 RPM. Next, the contents of the cylinder were left to settle for 1 h to remove large, non-stabilized particles. The supernatant was decanted into a round-bottom flask for solvent exchange in a rotary evaporator (1 h at 200 mbar).

The resulting inks were used without further processing. Thermogravimetric analysis (TGA 550 analyzer from TA Instruments) was used to determine the final ink composition. The inks consist of 9 wt% GNP, 27 wt% polymer (TPU, and EC) and 64 wt% solvent (M5-ink) and 4 wt% GNP, 13 wt% polymer and 82 wt% solvent (TEG-ink).

2.2. Ink characterization

The rheological behavior of the inks was characterized at 20 °C using an Anton Paar Physica MCR301 rheometer with a 25 mm parallel plate measurement system. The gap height was set to 1 mm for all measurements. For flow ramps, the shear rate $\dot{\gamma}$ was gradually increased from 0.001 to 1000 s^{-1}, while the viscosity was measured at 31 data points based on a ramp logarithmic duration from 60 s at the initial point to 3 s at the final point of 1000 s^{-1}. Amplitude sweeps were recorded at a frequency of 10 s^{-1} and a shear strain increasing from 0.01 – 100% in 25 steps with logarithmic spacing. In frequency sweeps, the shear amplitude was fixed at 0.01% (within the linear viscoelastic regime), while the frequency was varied from 0.1 – 100 rad/s. The storage and loss moduli were recorded at 16 intervals with logarithmic spacing. Finally, rotational peak-hold tests were executed, where the inks were held for 60 s at a shear rate of 0.1 s^{-1}, followed by a 60 s interval at 100 s^{-1} and 120 s at 0.1 s^{-1} to measure the viscosity recovery after shear release. A measurement was performed every 4 s.

In printing, the size of the largest particles sets the minimum nozzle size where nozzle clogging occurs. To obtain an estimate of the upper particle size limit in both inks, an Elcometer 2020 grind gauge with a range of 0 – 50 μm was used. For each ink, ten samples were taken, and the largest five particles per sample were recorded.

2.3. Experimental design

A three-factor Box-Wilson Central Composite Design (CCD3) with six center points was used for all four ink-nozzle combinations, followed by a two-factor CCD (CCD2) with five center points for the follow-up study with the 160 μm nozzle and the M5-ink [27,28]. Star points (alpha values) were located at ±1.68 for the CCD3 and ±1.41 for the CCD2 to ensure design rotatability [29]. The designs assume a second-order relationship between input and output variables. Designs were generated with the help of the Python package pyDOE2 [30] and the run order was randomized prior to printing. The full designs and an additional explanation are provided in section S3 of the supplementary information.

2.4. Printing

Direct ink writing was performed with a Hyrel 3D ENGINE HR high-resolution 3D printer equipped with a KR2 printhead, a stainless steel reservoir and Micron-S Precision Dispensing Tips (FISNAR®) with inner diameters of 60, 110, 160, 223, 335, 437, 564, 686 or 864 μm. Here, it should be noted that the FISNAR nozzles are available with inner diameters ranging from 60 μm – 1.04 mm. The Hyrel printer mechanically extrudes the ink via a screwing mechanism, on which further information can be found on the Hyrel wiki [31]. Details on the print settings can be found in section S2.1. Ink was deposited on TPU EU94 DS substrates (Delstar Technologies) which were placed on a vacuum stage. The zero z-position was manually calibrated using a flash light to determine the position where the nozzle touches the substrate.

The printer was operated from G-code files defining the test structures depicted in section S2.2. The test structures contained five repetitive structures, to efficiently obtain five duplications within one print. These G-code files were batch-generated with an in-house Python script. Besides the desired XY-translation for the print patterns (identical for all test structures), the G-code files contain operating conditions like the print speed F, standoff distance d and flow rate multiplier S and the actuator pulses required to extrude one μL of ink. While the first three parameters were varied within the CCDs, the number of pulses per μL was determined upfront for each ink as explained below. Priming and unpriming parameters were fixed at 2000 for all inks. A full print settings overview is included in section S3.2.

Preceding the DoE, extrudability tests were performed with both inks and a range of nozzles with inner diameters of 60, 110, 160, 223, 335, 437, 564, 686 and 864 μm. For these 2 m-long prints, the flow rate multiplier S was fixed at 1, the nozzle-to-substrate distance d was set to equal the nozzle diameter D, and the printing speed F was varied with D according to equation (4). The number of pulses per microliter P was set to 2000 in the extrudability tests, after which the actual P-value was determined by measuring the ink mass extruded in each of these extrudability tests (1612 and 1305 pulses/μL for the TEG- and M5-ink, respectively, see section S2.3). These experimentally obtained values were used in the CCD prints.

2.5. Print characterization

The print quality was scored by two independent operators based on four criteria (filament continuity, spacing, corner sharpness and reproducibility), which were each given a score 0–5 according to a scheme detailed in section S4. The overall quality score was subsequently determined according to the following formula:

$$\text{Quality} = \frac{\text{cont.} + \text{spacing} + \text{corners} + \text{repr.}}{20}, \tag{1}$$

where cont. abbreviates the line continuity and repr. the reproducibility.

A three-dimensional (3D) height profile was obtained for all five tracks of the test structure using a 3D optical profilometer (SensoFar PLμ2300). For each track, 101 focal planes were imaged along a height of 100 μm (160 μm nozzle), 200 μm (335 μm nozzle) or 400 μm (686 μm nozzle) and XY dimensions of ca 637 x 477 μm^2 for the 160 μm nozzle (pixel size: 0.83 μm/pixel) or ca 1.27 x 0.95 mm^2 for the 335 and 686 μm nozzles (pixel size: 1.65 μm/pixel). To extract filament base width, full-width-at-half-maximum (FWHM) and height (h) from the data, a 2D profile was extracted every twenty pixels, twenty profiles in total. These profiles were fitted numerically in MATLAB with a polynomial function to extract the metrics. The calculated values were first averaged across all sampling points per track. Finally, the results were averaged between the five tracks within each test structure. Hence, for each morphological output, there were five mean values per test run (= one print) resulting from twenty sampling points, which were averaged to obtain the final data point for this run in the CCD. The numerical method for response variable calculation was validated prior to implementation by comparing the results to manually collected data for a subset of 36 samples. Here, only an approximately 5% deviation was observed between the manually and numerically extracted values. Full details on the sampling and analysis procedures are included in the supplementary information (section S5.1). In addition, a detailed view of the top and cross-section of the printed structures has been obtained with scanning electron microscopy (SEM). Please see section S5.2 for further details.

Characterization of the filament resistance was performed with a Voltcraft VC840 multimeter over 4 cm-long line segments. To minimize the contact resistance, pieces of carbon film were placed between the test structures and the multimeter crocodile clips. Next, the conductivity σ was calculated according to $\sigma = l/(RA)$, with R the measured resistance, a segment length l = 40 mm and a cross-sectional area approximated as $A = \text{FWHM} \cdot h$.

2.6. Statistical analysis

For each CCD, a linear regression model was fitted to the coded dataset of each response variable in Python using the ordinary least squares (ols) function from the statsmodels package [32]. This regression model relates the responses to the printing parameters according to

$$\begin{aligned}\hat{y}_{\mathbf{z}} = {} & \hat{\gamma}_0 + \hat{\gamma}_A z_A + \hat{\gamma}_B z_B + \hat{\gamma}_C z_C + \hat{\gamma}_{AB} z_A z_B \\ & + \hat{\gamma}_{AC} z_A z_C + \hat{\gamma}_{BC} z_B z_C + \hat{\gamma}_{AA} z_A^2 \\ & + \hat{\gamma}_{BB} z_B^2 + \hat{\gamma}_{CC} z_C^2.\end{aligned} \tag{2}$$

Here, $\hat{y}_{\mathbf{z}}$ is the response variable, $\hat{\gamma}_i$ the regression coefficient of term i and z_i refers to the coded printing parameters defined as $z_i = (x_i - x_{i,0})/(0.5(x_{i,+} - x_{i,-}))$, with x_i the input factor in its original units, $x_{i,0}$ the factor center point and $x_{i,-}$ and $x_{i,+}$ the factor's −1 and +1 settings, respectively [27]. Terms with a p-value > 0.05 were iteratively eliminated from the model, unless they concerned a linear effect with a statistically significant higher-order counterpart (interaction or quadratic term) [29,27]. The resulting response surface models (RSMs) were finally visualized with respect to the uncoded variables in 3D plots.

2.7. Model validation and further improvement of print quality

To show the use of the response surface models in improving the print quality, a new set of prints was made with the 160 μm nozzle and the M5-ink. The prints were made according to a 2-factor CCD, varying the flow rate multiplier and nozzle-to-substrate distance within smaller ranges than in the previous 2-factor CCD, while fixing the printing speed at its intermediate value of 175 mm/min. The data were analyzed according to the same procedures described above. In addition, the data points were used to validate the predictions by the 3F CCD using the get_prediction function from the statsmodels package [32].

3. Results and discussion

To enable the reliable deposition of printed conductors using platelet-shaped materials, a workflow was developed which addresses the interplay between ink properties and the printing process (Fig. 1). The workflow consists of four steps: 1) determination of the printer design space including supported ink viscosities and nozzle sizes; 2) ink design and characterization, in particular filler size and ink rheology; 3) finding an overlap between the former two design spaces by selecting matching nozzle sizes that enable reliable ink extrusion; 4) print optimization within this overlapping design space using Design of Experiments (DoE) and smart test structures to a) obtain a general overview of print qualities and conductivities, and b) to perform detailed response surface modeling (RSM) of the properties of

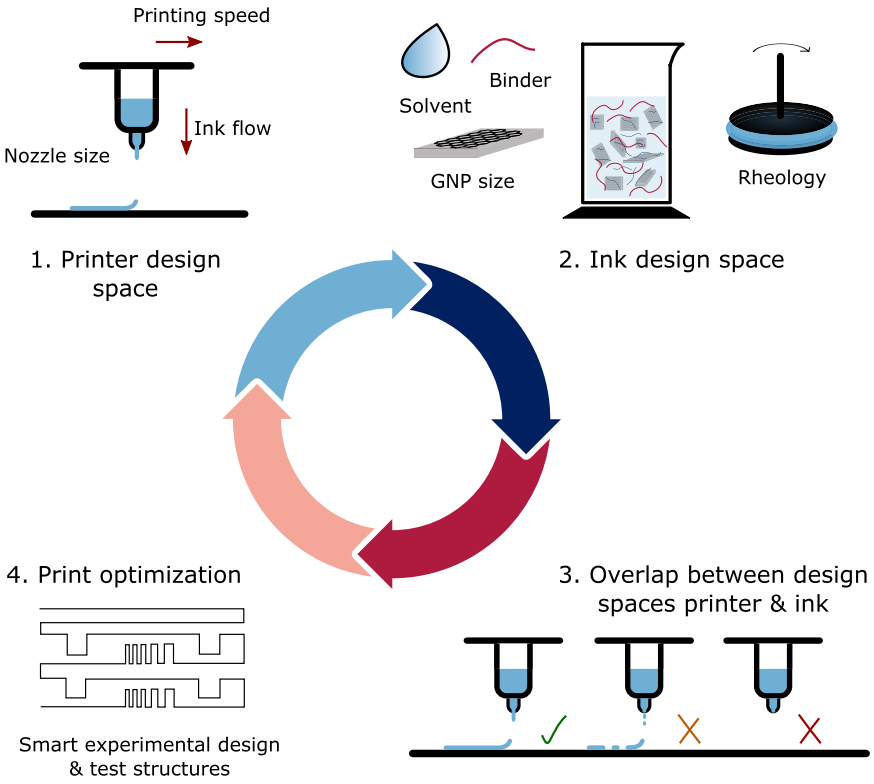

Fig. 1. Workflow for combined optimization of printer and ink parameters. 1) Printer boundary conditions such as nozzle sizes, pressure range and printing speed dictate ink design. 2) By adjusting the GNP colloid size, ink composition and rheology, printability over a wide window of printer parameters is ensured. 3) Ink extrudability through a range of nozzle sizes is tested to match the inks to nozzles of a maximum size range with extrusion potential. 4) Print quality optimization and print properties modeling is performed using Design of Experiments in combination with smart test structures to simultaneously optimize a range of printer parameters for two ink types and several nozzle diameters.

the deposited filaments: print quality, base width, full-width-at-half-maximum (FWHM) and height. If needed, the steps in this protocol may be repeated in an iterative manner, as recently also introduced for ceramics [33].

3.1. Printer design space

In the first step, the boundary conditions imposed by the printing system must be accounted for, such as the supported nozzle sizes, print speeds and ink viscosities. In this study, we opted for the Hyrel 3D ENGINE HR printer, which presents a good balance between cost, modularity (a wide range of supported ink viscosities (< 1000 Pa s), nozzle types and ink cartridges) and accuracy of deposition (1.25 μm in the XY- and 1.0 μm in the Z-direction). Additionally, this printing technology is currently gaining traction for a range of conditions and applications, ranging from printed electronics to tissue engineering, where 2D materials like GNPs and clay are frequently employed [34–36]. Therefore, optimization of the print conditions is relevant for a large scientific and engineering community. The Hyrel printer supports print speeds up to 15 mm/s and a range of flow rates. Based on the literature and some initial trials, three printing parameters were deemed most relevant for the printing process optimization: the nozzle-to-substrate distance d, the print speed F and the material flow rate multiplier S, which controls the ink flow rate at fixed print speed. Details on the selected print settings are included in the materials section and in section S3.

3.2. Ink design and characterization

The printer presented us with several boundary conditions for ink design, in particular platelet size and ink rheology. We tested nozzles with inner diameters D ranging from 60 – 864 μm, as our main interest was in printing structures between 0.1 – 1 mm. We aimed to maximize print resolution while benefiting from the conductivity provided by large GNPs. In this study, the aim was to use GNPs as conductive filler in a stretchable thermoplastic polyurethane (TPU) binder system, as this ink previously yielded electrodes with excellent conductivity, stretchability and durability after screen printing [4]. In platelet-based ink systems, the conductivity of the printed materials is, among others, determined by the filler flake size, for the conductivity is mainly limited by interplatelet junctions. This presents the user with a trade-off between conductivity and printability, e.g. nozzle clogging. To prevent nozzle blocking, the filler dimensions should ideally be below 1/100th or even 1/150th of the nozzle diameter [24,23]. This implies that for high-resolution printing of structures with a width of 100 μm, submicron sized fillers should be used, which seems not realistic for printing functional GNP-based conductive tracks.

Therefore, we set out to go beyond this nozzle-to-filler ratio limit. To this end, we formulated two inks based on different types of GNP fillers, the first one intended for highly conductive structures and the second ink suitable for printing of fine details. The first ink was made from in-house produced thermally expanded graphite (TEG) according to a previously published protocol [4], yielding GNP with a broad size distribution <50 μm. While the TEG-ink was expected to yield electrodes with maximum conductivity thanks to their large flake sizes, these large platelets were also expected to present issues with reliable deposition through small nozzles. Therefore, a second ink was produced from commercially available “M5” flakes with smaller size of approximately 5 μm and a lower polydispersity (M5). In the remaining text, the two inks are referred to as TEG-ink and M5-ink, respectively. As is shown in Fig. 2a and in the sections S1.2–S1.3, the two GNP types have rather different size distributions. While the M5-flakes have a relatively narrow size distribution centered around 5 μm, the TEG-flakes are much more poly-

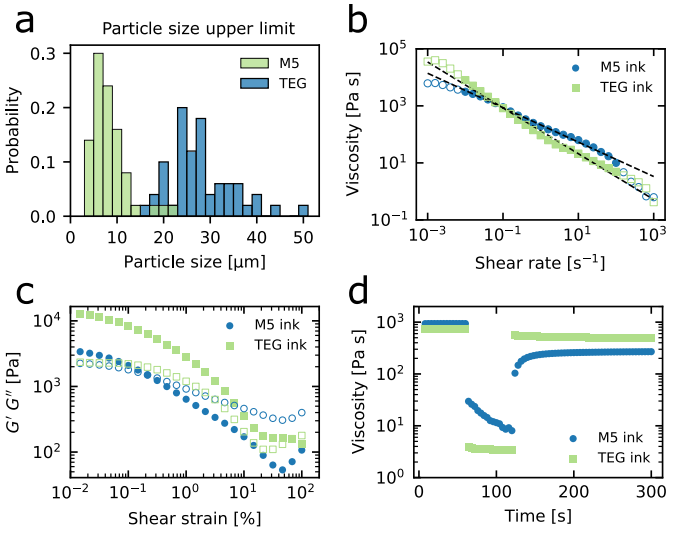

Fig. 2. Ink characterization of the M5- and TEG-inks. a) Particle size upper bound as determined from grind gauge measurements (10 per ink, the 5 largest particles per measurement); b) viscosity during shear rate sweeps with power law fits ($\eta = K\dot{\gamma}^{n-1}$ with K-values of 214 and 134, and n-values of 0.40 and 0.20 for the M5- and TEG-ink, respectively); c) amplitude sweeps (filled symbols denote the storage modulus G', while open symbols refer to the loss modulus G''); d) variation of the shear rate $\dot{\gamma}$ from 0.1 s^{-1} to 100 s^{-1} and back in a peak-hold test to measure elastic recovery of the viscosity.

disperse, with flakes ranging from submicron diameter to sizes beyond 20 µm.

For printability, the maximum filler size is more influential than the general size distribution. To get an impression of the upper particle limit in the inks, grind gauge measurements were performed. Each ink was sampled ten times, and the five largest particles per measurement are reported in Fig. 2a. From the size distributions, it can be concluded that the TEG-ink contains significantly larger particles than the M5-ink with a maximum of 50 vs 22 µm, and also a wider particle size distribution. In both cases, issues with nozzle obstruction could be foreseen for smaller nozzle sizes considering the guideline of an upper filler-to-nozzle-ratio of 1:100 (or 1:150) [24,23]. Hence, print optimization and careful selection of nozzle diameters is necessary.

As a consequence of the inks' diverging GNP sizes, M5- versus TEG-ink formulation required different levels of solid loading, while the ratio of GNP:TPU was maintained constant at 1:3. Thermogravimetric analysis (section S1.1) shows that the composition of the inks is 9 wt% GNP, 27 wt% polymer and 64 wt% solvent for the M5-ink versus or 4 wt% GNP, 13 wt% polymer and 82 wt% solvent for the TEG-ink. These formulations resulted in suitable rheologies for DIW. Note that the solvent is evaporated after printing, effectively resulting in identical ratios of filler-to-polymer matrix for both ink types. X-ray photoelectron spectroscopy (XPS) showed that the oxygen content of the M5- and TEG-flakes was around 5 and 4 wt% (section S1.4).

Rheology is crucial in DIW, for it determines both extrudability and shape fidelity [14,37,3,38,33]. Printing inks are generally viscoelastic, shear-thinning materials [37]. During extrusion, the high shear rates inside the nozzles are expected to align the platelet-shaped fillers, thereby reducing their viscosity. After deposition, the ink must return to a solid-like paste thanks to elastic recovery, which is crucial for shape fidelity [14,3]. Fig. 2 contains an overview of both the inks' rheological properties.

Here we employed flow ramps or shear rate sweeps to understand the rheology of printing inks. As is shown in Fig. 2b, both inks are clearly shear-thinning. Commonly, these viscosity versus shear rate data are fitted with a power law to extract the shear thinning index n, which is a measure for the extend of shear thinning [37,14,7]:

$$\eta = K\dot{\gamma}^{n-1}. \tag{3}$$

In this equation, η is the viscosity, K the flow consistency index and $\dot{\gamma}$ the shear rate. For shear thinning liquids, a shear thinning index $0 \leq n < 1$ should be observed, where the ink displays stronger shear thinning behavior when $n \to 0$. The curves in Fig. 2b are not perfectly linear, but to still get an indication of their degree of shear thinning, the log-transformed data points within the quasi-linear regime of 0.01 $\leq \dot{\gamma} \leq$ 100 s^{-1} were fitted. This yielded n-values of 0.40 and 0.20 for the M5- and TEG-ink, respectively. Hence, the TEG-ink is more shear thinning than the M5-ink.

Besides shear thinning, printing inks must be viscoelastic to achieve high print resolution. The inks' viscoelastic behavior was analyzed in oscillatory rheological tests. Fig. 2c shows the results of amplitude sweeps for both inks. At low shear strains, the flow behavior of both inks is predominantly solid-like, with the storage modulus dominating the loss modulus ($G' > G''$). Interestingly, the two inks behave differently under large strains. While the M5-ink displays a crossover point between G' and G'' around a shear strain of 0.2%, the TEG-ink behaves predominantly like a viscoelastic solid or gel over the entire strain amplitude range. This crossover point, also called flow point or yield stress, indicates that the M5-ink would also be suitable for three-dimensional DIW [14,3], which was however not the purpose of this study. In addition to the amplitude sweeps, frequency sweeps were performed (section S1.5). These indicated the relative frequency-independence of both the elastic and storage moduli, which is another indication of solid-like behavior, which favors shape-fidelity [37].

Finally, the time-dependent behavior (thixotropy) of the ink viscosity was studied in a peak-hold test or three intervals thixotropy test (3ITT). In these tests the inks were held at a close-to-static shear rate $\dot{\gamma} = 0.1$ s^{-1} for 60 s, after which the pastes were sheared at $\dot{\gamma} = 100$ s^{-1} for 60 s. Finally, the shear rate was reduced to $\dot{\gamma} = 0.1$ s^{-1}. As is shown in Fig. 2d, the ink viscosity recovers rapidly for both inks, but faster for the TEG-ink than for the M5-ink. Fast recovery of the viscosity is crucial for print resolution for it determines ink spreading on the substrate [39,14,40]. It was observed that the viscosity did not fully recover to its initial value, but this can likely be attributed to ink spill during the high shear interval [41].

To conclude, both inks display promising rheological properties for DIW, with some interesting differences in the degree of shear thinning, the presence or absence of a flow point and in the pace of elastic recovery after shear release. In addition, the filler size of both inks is different, dictating different requirements to the nozzle size and other print properties. In the next section, the selection of printing parameters is therefore discussed.

3.3. Overlap between design spaces of printer and ink

In the previous sections, the design spaces dictated by the printer and the inks were discussed. Next, the overlap between these design spaces must be determined. This ensures the print features within this superimposed design space can be efficiently optimized without many missing data points due to nozzle blocking. To determine the overlap in design space, an extrudability test was performed with the Hyrel 3D ENGINE HR high-resolution 3D printer. Extrudability is here defined as a measure for the predictability with which an ink is deposited through a circular nozzle of diameter D.

Generally, the print settings should be adapted to the ink rheology [33]. In this work, suitable printing speeds are determined by controlling the shear rate via the relation between viscosity and shear rate described by Equation (3):

$$F = \frac{4n}{3n+1}\frac{D^2\dot{\gamma}}{16Sr}, \tag{4}$$

with F the print speed, n the shear thinning index determined via Equation (3) (0.40 for the M5-ink and 0.20 for the TEG-ink), D the nozzle inner diameter, r the distance from the nozzle wall, and S the

Table 1
Reliability of filament extrusion through nozzles with various inner diameters. The reliability was determined by line continuity and consistency and ranged from high (++) to intermediate (+ −) to poor (− −). A zero score (0) indicates no ink deposition. FTNR abbreviates the upper filler-to-nozzle ratio, calculated based on the largest GNP sizes (22 μm in the M5-ink and 50 μm in the TEG-ink).

Nozzle D [μm]	M5		TEG	
	FTNR	Extrusion	FTNR	Extrusion
60	1/3	0	1	0
110	1/5	− −	1/2	0
160	1/7	++	1/3	0
223	1/10	++	1/4	− −
335	1/15	++	1/7	+ −
437	1/20	++	1/9	+ −
564	1/26	++	1/11	++
686	1/31	++	1/14	++
864	1/40	++	1/18	++

dimensionless flow-rate multiplier, which dictates the flow rate without changing the printing speed. Equation (4) sets the print speed when printing an ink with a given shear thinning index through a nozzle with diameter D while maintaining a target shear rate of $\dot{\gamma}$ at a distance r from the nozzle wall. While both S and F influence the ink flow, only S allows for adjusting the flow without changing the print speed. The derivation of Equation (4) is provided in section S2.4. Based on some initial trials, we aimed for a shear rate of 100 s^{-1} at $r = D/4$ for the M5-ink and 67 s^{-1} at the same position in the nozzle for the TEG-ink. The target shear rate was higher for the M5-ink, because of the lower degree of shear thinning of this ink and because preliminary experiments had taught us that the M5-ink could handle fairly high shear rates without leakage.

A two meter-long test structure was printed with all ink-nozzle combinations displayed in Table 1, with nozzle inner diameters D ranging from 60 to at least 864 μm. In this series of experiments, the printing speed F was varied with the nozzle diameter according to equation (4), while the nozzle-to-substrate distance d was set equal to D. The prints were visually evaluated on the basis of deposition quality on a TPU substrate. The quality herein was determined by line continuity and consistency and ranged from high (++) to intermediate (+ −) to poor (− −). When no ink was deposited, the extrudability would receive a zero score (0). The results are presented in Table 1. Reliable deposition was observed from nozzles with sizes ranging from 160 to 864 μm, where the M5-ink allowed for reliable extrusion through smaller nozzles down to 160 μm (maximum filler-to-nozzle ratio of 1/7), while the TEG-ink required nozzles of at least 335 μm in diameter (also a maximum filler-to-nozzle ratio of 1/7) to obtain somewhat (+ −) reliable deposition. For smaller nozzles approaching a maximum filler-to-nozzle ratio of 1/5, clogging became an issue, which would prevent the meaningful interpretation of print results in an optimization setting. Expectedly, nozzle clogging proved more of an issue for the TEG-ink than for its M5 counterpart, which can be explained by the larger particle sizes of this ink as well as reduced ink stability.

Together, the M5- and TEG-inks cover a large part of the printer design space: nozzle sizes of 160 – 864 μm. Herein, the M5-ink is particularly suited for high resolution printing, while the TEG-ink provides higher conductivity. To use the entire printer design space down to 60 μm, an ink containing even finer colloids would be required. Next, we aimed to explore the realistically achievable print space in more detail with four combinations of inks and nozzle sizes selected from the initial screening. For the M5-ink, the 160 and 335 μm nozzles were selected, and for the TEG-based ink the 335 and 686 μm nozzles. This choice allowed us to compare printed structures between the two inks, while also studying the effect of doubling the nozzle diameter on the print quality.

3.4. Printing process optimization

For production of functional materials like printed electronics, control over the filament morphology, i.e. width and height, as well as conductivity are important. As the focus of this study was on printing electronics with high resolution, we were particularly interested in overall print quality (i.e. filament continuity, line spacing, corner sharpness and reproducibility), filament morphology (i.e. height, base width and FWHM), and conductivity. To develop a predictive understanding of the realistically achievable print space, a Design of Experiments (DoE) approach was taken.

Based on the literature and some initial trials, three printing process parameters were deemed most relevant for the printing process optimization: 1) the nozzle-to-substrate distance d, 2) the printing speed F, which governs the shear rate and the flow rate as is discussed in more detail in section S2.4, and 3) the material flow rate multiplier S, which controls the ink flow rate at fixed printing speed. With two inks, two nozzle diameters per ink, three printing parameters and five outputs of interest (print quality, height, FWHM, base width and conductivity), the number of experiments for a statistically reliable dataset could easily become overwhelming. Therefore, we opted for smart sampling with Design of Experiments (DoE) and efficient test structures to limit the number of prints. DoE offers a systematic approach to engineering problem solving by designing the data collection stage such that statistically valid conclusions can be drawn based on a minimum expenditure of resources [27,29]. This is achieved by sampling a carefully drafted subset of the design space.

For each nozzle and ink combination, we employed a three-factor central composite design (CCD). This design consists of twenty runs (prints) per experiment, which are formed by combinations of five setting levels per input variable (Table 3). The factor settings are linearly spaced such that the five settings correspond to scaled values of -1.68, -1, 0, +1, +1.68. From these scaled values, the factor settings for each nozzle size and ink were calculated (Table 2). The full designs and a detailed explanation can be found in Table 3 and in section S3. After randomization of the run order, each set of input variables was entered into a G-code file, i.e. a code file with commands read by the printer, and a smart test structure as shown in Fig. 3 was printed. These test structures contained several important features such as linear tracks for conductivity measurements, corners to test corner sharpness, lines with decreasing spacing and five duplicate structures within one print. Finally, the results were used to create response surface models (RSMs) using linear regression, which provide a guide on how to change print settings to achieve a specific print morphology and conductivity.

As a first evaluation of print quality, a quality assessment was performed based on four evaluation criteria: filament continuity, line spacing, corner sharpness and reproducibility. This quality scoring already reveals large differences between prints, as is shown in Fig. 3. Hence, it may be concluded that print settings have an enormous effect on print quality, even when the ink and nozzle are fixed. Across all CCDs, a significant proportion of prints has a relatively low quality score < 0.5. From Fig. 3, print quality is higher and more uniform for the larger nozzle size for each respective ink, which can be attributed to reduced nozzle clogging due to a reduction in filler-to-nozzle ratio. In Fig. 3, panels b-e provide the distribution of scores for each of the four quality components for the four ink-nozzle combinations. These charts indicate that continuity and spacing provide the largest challenge within this design space. A lack of continuity may be due to ink inhomogeneity, i.e. nozzle blocking due to large platelets. Interestingly, overall quality distributions are similar for both inks, despite the M5-ink being used in combination with smaller nozzles. This is likely due to the filler-to-nozzle ratios being similar between the M5/160 and TEG/335 ink-nozzle combinations and the M5/335 and TEG/686 ink-nozzle com-

Table 2
Printing process parameters varied in the central composite designs (CCDs) at the −1.68, −1, 0, +1 and +1.68-levels. FTNR abbreviates the upper filler-to-nozzle ratio, calculated based on the largest GNP sizes (22 μm in the M5-ink and 50 μm in the TEG-ink).

Ink & nozzle	FTNR	Print speed F [mm/min]	Standoff distance d [mm]	Flow rate multiplier S [-]
M5 & 160 μm	1/7	28, 87, 175, 262, 322	0.08, 0.12, 0.17, 0.22, 0.26	0.159, 0.5, 1.0, 1.5, 1.84
M5 & 335 μm	1/15	58, 183, 366, 549, 674	0.17, 0.24, 0.36, 0.47, 0.54	0.159, 0.5, 1.0, 1.5, 1.84
TEG & 335 μm	1/7	27, 84, 169, 253, 310	0.17, 0.29, 0.47, 0.64, 0.76	0.159, 0.5, 1.0, 1.5, 1.84
TEG & 686 μm	1/14	55, 173, 345, 518, 635	0.34, 0.59, 0.95, 1.31, 1.56	0.159, 0.5, 1.0, 1.5, 1.84

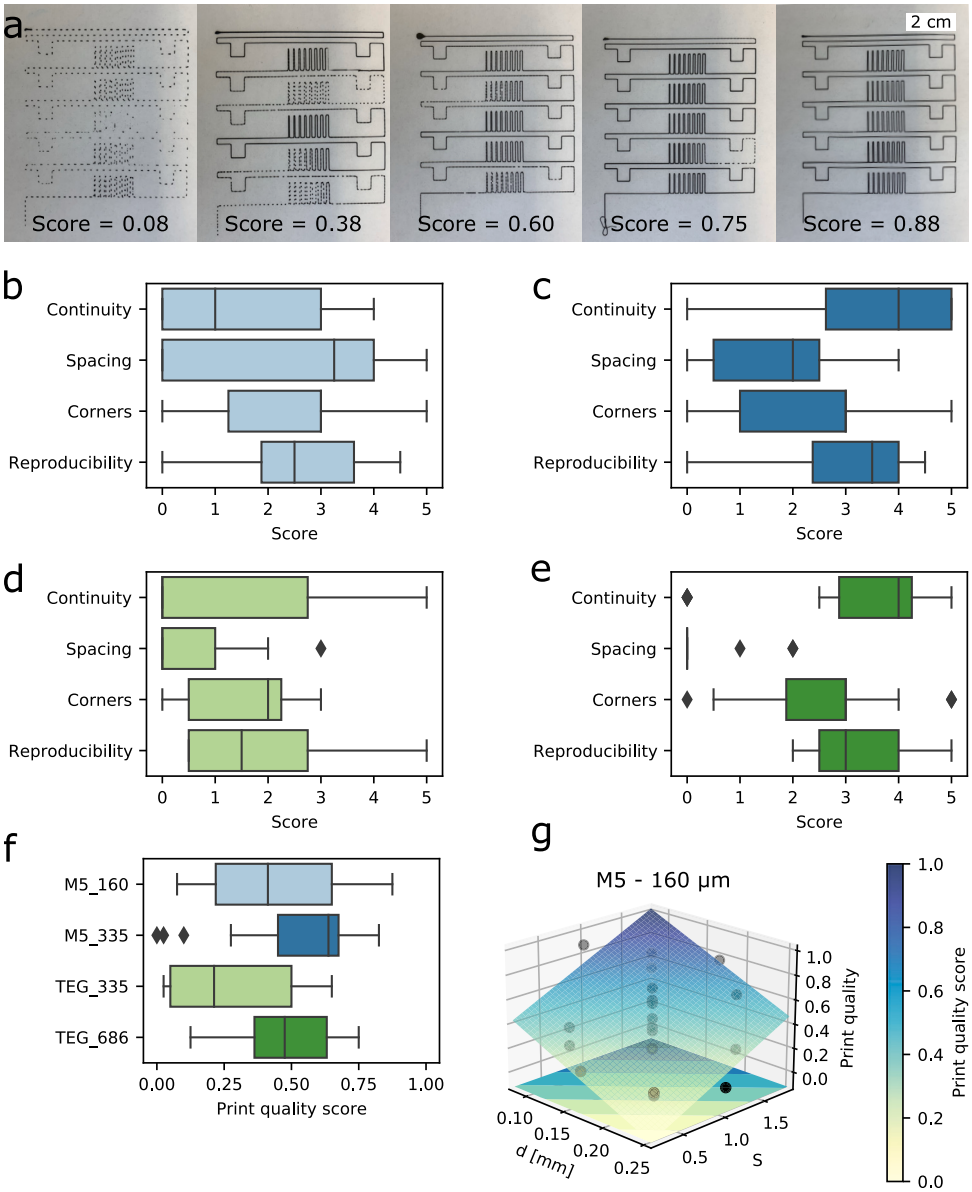

Fig. 3. Print quality of prints across the four central composite designs. a) Example prints across the quality range obtained with the M5-ink and the 160 micrometer nozzle combination; scores obtained f.l.t.r.: 0.08, 0.38, 0.60, 0.75 and 0.88; scale bar: 2 cm (full print width: 6 cm); b-e) Score distributions for each of the four quality criteria (continuity, spacing, corner sharpness & reproducibility) for b) M5-ink with 160 μm nozzle; c) M5-ink with 335 μm nozzle; d) TEG-ink with 335 μm nozzle; e) TEG-ink with 686 μm nozzle; f) overall print quality score for the four ink-nozzle combinations; g) response surface model for the M5-ink with 160 μm nozzle at F = 175 mm/min, with the CCD data points plotted in black. Diamond symbols correspond to outliers (beyond 1.5 times the interquartile range less than the first quartile or greater than the third quartile).

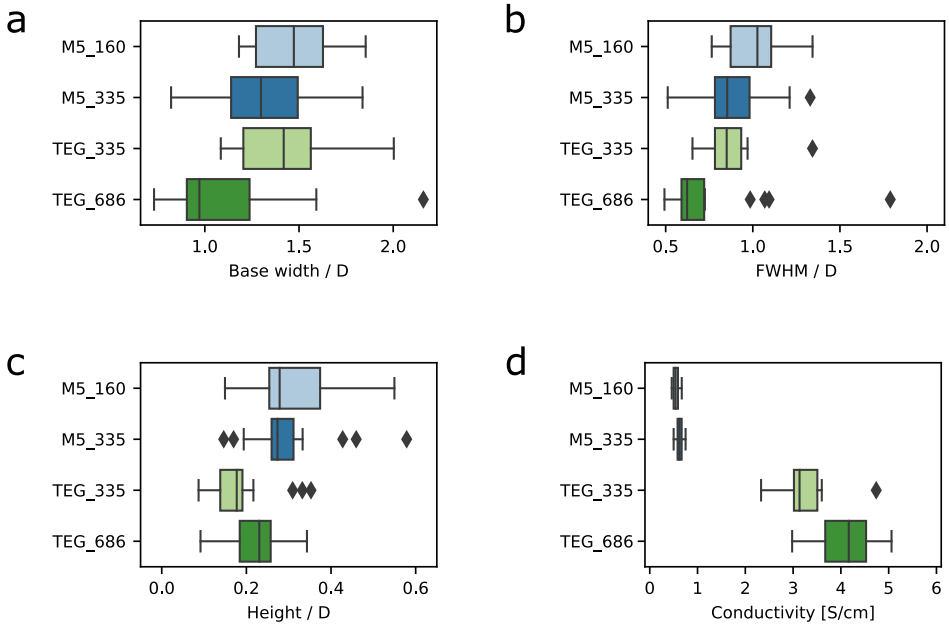

Fig. 4. Properties of the dried filaments for the four ink-nozzle combinations; a) filament base width normalized by the nozzle diameter D; b) normalized full-width-at-half-maximum (FWHM); c) normalized filament height; d) conductivity. Diamond symbols in panels d-f correspond to outliers (beyond 1.5 times the interquartile range less than the first quartile or greater than the third quartile).

Table 3
Three-factor central composite designs (CCDs) used in this study. The print order was randomized afterwards for each CCD.

Print	Factor A (F)	Factor B (d)	Factor C (S)
1	−1	−1	−1
2	+1	−1	−1
3	−1	−1	+1
4	+1	−1	+1
5	−1	+1	−1
6	+1	+1	−1
7	−1	+1	+1
8	+1	+1	+1
9	0	0	0
10	0	0	0
11	0	0	0
12	−1.68	0	0
13	+1.68	0	0
14	0	0	−1.68
15	0	0	+1.68
16	0	−1.68	0
17	0	+1.68	0
18	0	0	0
19	0	0	0
20	0	0	0

binations (Table 2). When comparing the two inks with the same nozzle diameter (335 μm), the print quality is indeed higher and more uniform for the M5-ink. This confirms that the M5-ink is more suitable for high-resolution printing than the TEG-ink. The results suggest that the further the filler-to-nozzle ratio is reduced, the closer one gets to a continuum with predictable deposition results.

Besides diverging print qualities, the four CCD design spaces also resulted in a large library of print morphologies and conductivities. The filaments were characterized in three dimensions using 3D optical profilometry (section S5.1) and SEM (section S5.2). The response variables filament base width, full-width-at-half-maximum height (FWHM) and height were extracted from the profilometer data in an automated fashion as detailed in sections 2.5 and S5.1. In Fig. 4, the response variables are normalized with respect to the nozzle diameter for comparability across nozzles.

Fig. 4 and Table 4 provide an overview of the morphologies obtained for the four CCDs. The results clearly indicate that even with a fixed type of nozzle and ink still variations in print dimension of a factor four can be achieved. Notably, base widths below the nozzle diameter have been obtained for the 335 μm nozzle (M5-ink) and 686 μm nozzle (TEG-ink). Importantly, this is the first demonstration of sub-nozzle diameter printing for 2D materials. This achievement is in line with an earlier example of sub-nozzle diameter printing for spherical colloids with a much lower filler-to-nozzle ratio than in the current work [42]. While the print quality in these cases was limited, sub-nozzle diameter printing will be further discussed in the next section, where the print quality could be significantly improved within a second print iteration.

FWHM and in particular height values are generally lower for lines printed with the TEG-ink than with the M5-ink. This might be explained by the increased solvent content of this ink. In addition, solvent outflow caused by increased colloidal instability and the broad size distribution of the TEG-ink compared to the M5-ink might have contributed to the decreased print heights, for this solvent drag carried along some smaller flakes as indicated by optical profilometry (section S5.3). Interestingly, while a statistically significant correlation exists between filament height and FWHM for the aggregate dataset of the four ink-nozzle combinations, the adjusted R^2 is low with a value of 0.12. These results suggest that height and FWHM can be tuned (quasi) independently. In contrast, FWHM turns out to be an excellent predictor of base width, with adj. $R^2 = 0.89$ (section S6).

Filament conductivity σ was calculated from two-point resistance measurements on the dried filaments. The filaments produced from the TEG-ink (3.1 ± 0.51 S/cm for the 335 μm nozzle) displayed an approximately five-fold higher conductivity than their M5-counterparts (0.62 ± 0.071 S/cm for the 335 μm nozzle). This difference can be mainly attributed to the larger platelet size of the TEG-GNP, because GNP-to-GNP junctions are likely the main contributor to the increased resistivity of GNP-based composites relative to the in-plane conductivity of pristine graphene (up to 10^5 S/m) [43–45]. Increasing the number of

Table 4
Print properties spanned by the CCD design spaces.

Ink	D [μm]	Base width [μm]	FWHM [μm]	Height [μm]	Conductivity [S/cm]
M5	160	189 – 297	122 – 215	35 – 63	0.46 – 0.67
M5	335	275 – 615	172 – 445	68 – 126	0.50 – 0.75
TEG	335	363 – 671	220 – 450	41 – 102	2.2 – 4.0
TEG	686	529 – 1482	338 – 1227	101 – 308	3.0 – 4.9

Table 5
Sensitivity of the various outputs to each of the input parameters, interactions and quadratic terms. For each linear model, the regression coefficients have been normalized with respect to the largest term. Only statistically significant parameters ($p < 0.05$) are included. A negative number denotes an inverse correlation. Factor A encodes printing speed, factor B the flow rate multiplier and factor C the standoff distance.

CCD	Output	A	B	C	A^2	B^2	C^2	AB	AC	BC	adj. R^2
3F-160-M5	Print quality	0.60	1.0	−0.97							0.75
	Height	−0.79	1.0		0.55			0.69			0.73
	FWHM		1.0								0.46
	Base width		1.0								0.45
3F-335-M5	Print quality	0.39	1.0	−0.61	−0.46	−0.76				−0.55	0.92
	Height	−0.17	1.0	0.15		−0.23		0.13		0.18	0.95
	FWHM	0.11	1.0	−0.11	−0.08					−0.09	0.99
	Base width		1.0	−0.17							0.89
3F-335-TEG	Print quality	0.51	1.0	−0.61							0.64
	Height		−1.0								0.53
	FWHM	1.0			0.41	0.66		0.88			0.68
	Base width	−0.96	0.69	−0.52	0.65			1.0			0.73
3F-686-TEG	Print quality		0.95	−1.0		−0.84			−0.97	0.84	0.71
	Height		1.0	0.67	−0.38	−0.45	−0.34			0.57	0.88
	FWHM		1.0	−0.66			0.45			−0.38	0.93
	Base width		1.0	−0.49							0.65

junctions by using smaller GNPs will therefore increase the resistance. SEM images (section S5.2) clearly indicate that smaller nanoplatelets result in a finer network, which can be linked to more contact points. Furthermore, as polymeric chains adhere to the GNP surface, the distance over which electron transfer must occur is beyond the maximum tunneling distance. The number of GNP-to-GNP junctions and the increased interplatelet spacing introduced by the attached polymers could explain the lower conductivity of the M5-ink.

Within the range of print conditions in this study, the conductivity appears close-to-constant across nozzle sizes for the M5-ink. In contrast, the conductivity distributions for the TEG prints are dependent on the nozzle used, with the larger nozzle yielding higher conductivities. We hypothesize this is due to an increasing number of print imperfections when employing a smaller nozzle, where increasing filler-to-nozzle ratios lead to the continuum model for a conductor to break down. As shown elsewhere, the conductivity values could be further improved by post-treatment with photonic annealing [4]. The resistance displayed a linear correlation with the reciprocal area, meaning that it can be predicted from the morphological features, or vice versa (section S7). Therefore, it was not necessary to include the conductivity in the response surface modeling below.

Utilizing the full predictive capabilities of the used experimental approach based on DoE, a response surface model (RSM) was fitted to each of the outputs (print quality, filament base width, FWHM and height) for all data sets using least squares ordinary regression. The supplementary information (section S8) contains the full set of regression coefficients. A sensitivity analysis was performed to assess the relative sensitivity of the output parameters to the three input factors and their interactions based on the regression coefficients. The results in Table 5 show that the flow rate multiplier has a large effect on both the print quality and the print morphology. Yet, in most cases also the printing speed and the nozzle-to-substrate distance affect the print quality and/or the filament dimensions. It can be concluded that the print results are generally a product of interplay between the three printing process parameters. Altogether, the three parameters capture a large share of the variation in the output data, as is indicated by the high adjusted R^2 values of the models (Table 5).

A few example response surfaces are highlighted in Fig. 3f and Fig. 5, with the full set included in section S8. Fig. 5 shows the response surfaces of the morphological features for the smallest and largest nozzles in this study. Even for a fixed combination of nozzle size and ink type, a wide range of print dimensions can be obtained. These models visualize the influence of the printing process parameters on the filament properties. Depending on the initial choice of parameters, the maximum and/or minimum feature size is captured by the respective RSM. For instance, the model for the 686 μm nozzle (TEG-ink) in Fig. 5c predicts a maximum filament height of 358 μm at $F = 364$ mm/min, $S = 1.8$ and $d = 1.6$ mm (note that this maximum is shifted with respect to panel 5c due to the RSM being plotted at a standoff distance of $d = 0.95$ mm instead of 1.6 mm). In other cases, like in panels a, b and d, the RSMs captured the direction of trends while not containing a peak or valley. Together with the print quality RSM in Fig. 3f, this figure illustrates the use of the response surface models in optimization of the print quality and achieving specific filament dimensions required for a target application. The predictive models in this study are specific to four design spaces set by fixed ink-nozzle combinations. In the future, this may be extended by suitable machine learning approaches such as transfer learning, which demonstrated for aerosol jet printing that the

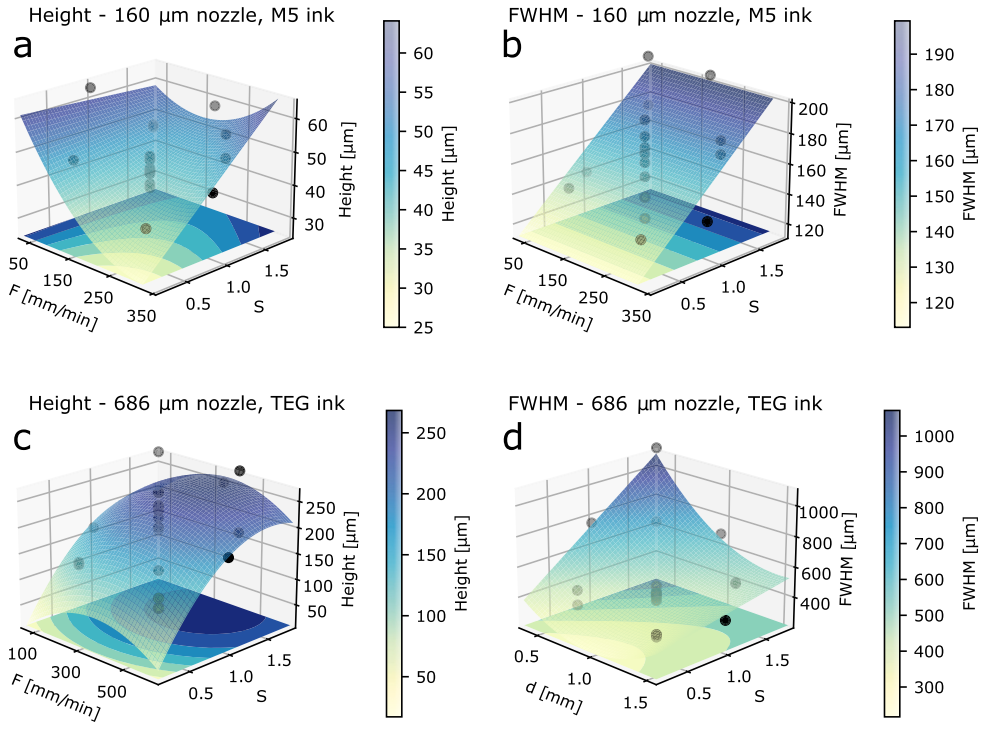

Fig. 5. Selection of response surface models (RSMs) describing the morphological features of prints made with the 160 µm nozzle and M5- ink (a-b) or the 686 µm nozzle and TEG-ink (c-d); a) height with d = 0.169 (adj. R^2 = 0.73); b) FWHM with d = 0.169 (adj. R^2 = 0.46); c) height with d = 0.951 (adj. R^2 = 0.88); d) FWHM with F = 345 mm/min (adj. R^2 = 0.93); The dots represent the CCD data points.

ideal operating windows could be predicted beyond the boundaries of the measured space [46].

3.5. Iterative print quality optimization and model validation

To highlight the importance of response surface modeling and to illustrate that optimization can be done in an iterative manner for the best print resolution and deposition quality, the print quality response surface for the 160 µm nozzle with the M5-ink in Fig. 3f was used as a guidance for a new set of prints with improved print quality. The overall print quality of the original dataset was fairly low (average print quality score < 0.5), with the model indicating that the print quality is highest at low standoff distances and high flow rate multiplier values. Therefore, a two-factor follow-up study was designed with a new range of lower standoff distances. The printing speed was fixed at the intermediate value of 175 mm/min, for it was the least influential input parameter with respect to the print quality. The flow rate multiplier was still varied similarly as before to ensure sufficient morphological variability in the output data.

The results of this second iteration were truly impressive. As is shown in Fig. 6a and in section S4.3, the print quality improved drastically with respect to the first set of prints, with the mean quality shifting from 0.44 ± 0.25 to 0.82 ± 0.13. In addition, the new set of prints contained filaments with base widths of sub-nozzle diameter dimensions (118, 133 and 152 µm). As an example, where high print resolution is needed, we are also providing some example prints for supercapacitor electrodes that were obtained with a 160 µm nozzle (section S9). Linear regression demonstrates that both the base width and FWHM can be reduced by lowering the flow rate multiplier S. However, S cannot be lowered infinitely, as at some point the print quality is sacrificed (see the response surface in section S8.5). While the 152 and 133 µm wide prints (FWHM: 104 and 86 µm) had excellent or good quality (print quality scores of respectively 0.90 and 0.70), the 118 µm wide print (FWHM 77 µm) had a lower score of only 0.50. This shows that understanding and tuning of the printing process requires an integrated approach which considers multiple printing parameters and outputs. When done successfully, such an approach provides access to a large design space, while the response surface models provide a useful guidance in navigating this space.

Finally, the second set of prints was used to validate the results of the initial models. For each output, the predicted values were compared to their measured counterparts in the 2F CCD. Only four data points of the CCD could be used for this purpose, as only those four points fell within the parameter ranges spanned by the original study, while CCD models do not account for extrapolation. The results are shown in Fig. 6 and in section S8.4. For all four outputs (print quality, height, FWHM and base width), the four data points fall within the prediction interval of the regression models. For instance, panel b of Fig. 6 shows the predicted FWHM versus their predicted values. While the model has excellently captured the trend in the validation data, it overpredicts the width. This might be attributed to an offset in the z-position calibration of the Hyrel printer. It would have likely been easier to validate the models of the larger nozzle sizes, which thanks to their larger diameter and consequently larger nozzle-to-substrate distances are less sensitive to the z-calibration. However, as the focus of this work was on high-resolution printing, it was decided to validate the most challenging set of models for the smallest nozzle.

4. Conclusion

In this study, we demonstrated the feasibility of high-resolution direct ink writing of inks containing graphene nanoplatelets as conductive fillers with a high filler-to-nozzle size ratio. We developed a workflow for the integrated optimization of ink rheology and printing process parameters to predict and tune filament quality and morphology. Using two inks with diverging rheologies and filler sizes, and three nozzle diameters, we have printed filaments with a wide range of dimensions and conductivities suitable for application in sensors or electrodes. Moreover, we have developed predictive models which were successfully used to predict filament dimensions. Moreover, the predictive models

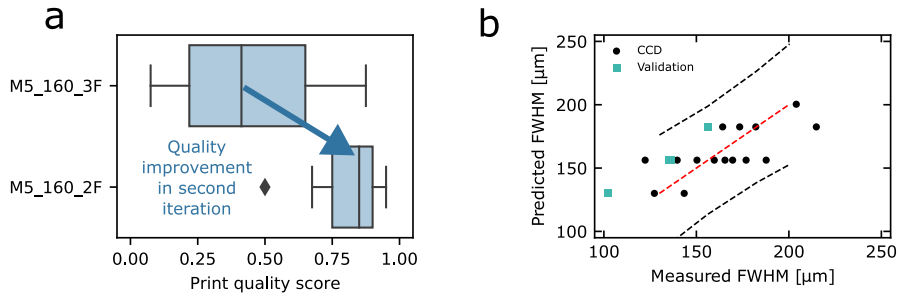

Fig. 6. Follow-up two-factor (2F) central composite design to improve the print quality with the 160 µm nozzle and M5-ink; a) print quality improvement relative to the initial three-factor (3F) CCD ; b) measured FWHM in the 2F CCD and the 3F CCD versus the values predicted by the 3F CCD (red dashed curve). The black dashed curves represent the prediction interval. The diamond symbol in panel a corresponds to an outlier (beyond 1.5 times the interquartile range less than the first quartile).

were deployed to achieve excellent print quality within one iteration of the workflow, despite the large filler dimensions with a challenging filler-to-nozzle size ratio of 1/7. As DIW of platelet-based inks is gaining traction in several fields, this study will benefit high-resolution rapid prototyping of a large class of functional materials for wearable electronics, sensors, RF passives, energy materials and tissue engineering.

Declaration of competing interest

The authors declare that they have no known competing financial interests or personal relationships that could have appeared to influence the work reported in this paper.

Data availability

The raw data required to reproduce these findings are available to download from the 4TU.ResearchData Repository [47]. The processed data required to reproduce these findings are available to download from the 4TU.ResearchData Repository [47].

Code availability

The code required to reproduce these findings is available to download from the 4TU.ResearchData Repository [47].

Acknowledgements

Dr. Jeroen Sol is acknowledged for help with the Hyrel system. Dr. Stefan Govers is thanked for the XPS measurements. Marc van Maris of the Multi-scale lab is acknowledged for technical support during the profilometry measurements. This project has received funding from the European Union's Horizon 2020 research and innovation programme under grant agreement No 881603 (Graphene Flagship Core 3).

Appendix A. Supplementary material

Supplementary material related to this article can be found online at https://doi.org/10.1016/j.apmt.2023.102014.

References

[1] A. Kamyshny, S. Magdassi, Conductive nanomaterials for 2D and 3D printed flexible electronics, Chem. Soc. Rev. 48 (6) (2019) 1712–1740, https://doi.org/10.1039/C8CS00738A.
[2] G. Hu, J. Kang, L.W. Ng, X. Zhu, R.C. Howe, C.G. Jones, M.C. Hersam, T. Hasan, Functional inks and printing of two-dimensional materials, Chem. Soc. Rev. 47 (9) (2018) 3265–3300, https://doi.org/10.1039/C8CS00084K.
[3] S. Tagliaferri, A. Panagiotopoulos, C. Mattevi, Direct ink writing of energy materials, Mater. Adv. 2 (2) (2021) 540–563, https://doi.org/10.1039/d0ma00753f.
[4] L.S. van Hazendonk, A.M. Pinto, K. Arapov, N. Pillai, M.R.C. Beurskens, J.-P. Teunissen, A. Sneck, M. Smolander, C.H.A. Rentrop, P.C.P. Bouten, H. Friedrich, Printed Stretchable Graphene Conductors for Wearable Technology, Chem. Mater. 34 (17) (2022) 8031–8042, https://doi.org/10.1021/acs.chemmater.2c02007.
[5] S. Afroj, S. Tan, A.M. Abdelkader, K.S. Novoselov, N. Karim, Highly conductive, scalable, and machine washable graphene-based e-textiles for multifunctional wearable electronic applications, Adv. Funct. Mater. 30 (23) (2020) 2000293, https://doi.org/10.1002/adfm.202000293.
[6] H. Zhang, S.K. Moon, Reviews on Machine Learning Approaches for Process Optimization in Noncontact Direct Ink Writing, ACS Appl. Mater. Interfaces 13 (45) (2021) 53323–53345, https://doi.org/10.1021/acsami.1c04544.
[7] H.A. Loh, A.R. Graves, C.D. Stinespring, K.A. Sierros, Direct Ink Writing of Graphene-Based Solutions for Gas Sensing, ACS Appl. Nano Mater. 2 (7) (2019) 4104–4112, https://doi.org/10.1021/acsanm.9b00572.
[8] E. Caffrey, J.R. Garcia, D. O'Suilleabhain, C. Gabbett, T. Carey, J.N. Coleman, Quantifying the Piezoresistive Mechanism in High-Performance Printed Graphene Strain Sensors, ACS Appl. Mater. Interfaces 14 (5) (2022) 7141–7151, https://doi.org/10.1021/acsami.1c21623.
[9] S. Afroj, N. Karim, Z. Wang, S. Tan, P. He, M. Holwill, D. Ghazaryan, A. Fernando, K.S. Novoselov, Engineering graphene flakes for wearable textile sensors via highly scalable and ultrafast yarn dyeing technique, ACS Nano 13 (4) (2019) 3847–3857, https://doi.org/10.1021/acsnano.9b00319.
[10] H. Zhang, R. He, Y. Niu, F. Han, J. Li, X. Zhang, F. Xu, Graphene-enabled wearable sensors for healthcare monitoring, Biosens. Bioelectron. 197 (2022) 113777, https://doi.org/10.1016/j.bios.2021.113777.
[11] S.D. Kim, A. Sarkar, J.-H. Ahn, Graphene-Based Nanomaterials for Flexible and Stretchable Batteries, Small (2021) 2006262, https://doi.org/10.1002/smll.202006262.
[12] K. Arapov, K. Jaakkola, V. Ermolov, G. Bex, E. Rubingh, S. Haque, H. Sandberg, R. Abbel, G. de With, H. Friedrich, Graphene screen-printed radio-frequency identification devices on flexible substrates, Phys. Status Solidi 10 (11) (2016) 812–818, https://doi.org/10.1002/pssr.201600330.
[13] A. Lamminen, K. Arapov, G. de With, S. Haque, H.G. Sandberg, H. Friedrich, V. Ermolov, Graphene-flakes printed wideband elliptical dipole antenna for low-cost wireless communications applications, IEEE Antennas Wirel. Propag. Lett. 16 (2017) 1883–1886, https://doi.org/10.1109/LAWP.2017.2684907.
[14] A. Corker, H.C.-H. Ng, R.J. Poole, E. García-Tuñón, 3D printing with 2D colloids: Designing rheology protocols to predict 'printability' of soft-materials, Soft Matter 15 (6) (2019) 1444–1456, https://doi.org/10.1039/C8SM01936C.
[15] H. Ding, S. Barg, B. Derby, Direct 3D printing of graphene using capillary suspensions, Nanoscale 12 (21) (2020) 11440–11447, https://doi.org/10.1039/C9NR10831A.
[16] R. Haney, P. Tran, E.B. Trigg, H. Koerner, T. Dickens, S. Ramakrishnan, Printability and performance of 3D conductive graphite structures, Addit. Manuf. 37 (2021) 101618, https://doi.org/10.1016/j.addma.2020.101618.
[17] M.A.S.R. Saadi, A. Maguire, N.T. Pottackal, M.S.H. Thakur, M.M. Ikram, A.J. Hart, P.M. Ajayan, M.M. Rahman, Direct Ink Writing: A 3D Printing Technology for Diverse Materials, Adv. Mater. 34 (28) (2022) 2108855, https://doi.org/10.1002/adma.202108855.
[18] A.C.H. Tsang, J. Zhang, K.N. Hui, H. Huang, Recent Development and Applications of Advanced Materials via Direct Ink Writing, Adv. Mater. Technol. (2022) 2101358–2101389, https://doi.org/10.1002/admt.2021013.
[19] X. Yan, Y. Tong, X. Wang, F. Hou, J. Liang, Extrusion-Based 3D-Printed Supercapacitors: Recent Progress and Challenges, Energy Environ. mater. 5 (3) (2022) 800–822, https://doi.org/10.1002/eem2.12260.
[20] H. Yuk, X. Zhao, A New 3D Printing Strategy by Harnessing Deformation, Instability, and Fracture of Viscoelastic Inks, Adv. Mater. 30 (6) (2018) 1704028, https://doi.org/10.1002/adma.201704028.
[21] R. Tandel, B.A. Gozen, Direct-Ink-writing of liquid metal-graphene-based polymer composites: Composition-processing-property relationships, J. Mater. Process. Technol. 302 (2022) 117470, https://doi.org/10.1016/j.jmatprotec.2021.117470.

[22] N. Divakaran, J.P. Das, A.K.P. V, S. Mohanty, A. Ramadoss, S.K. Nayak, Comprehensive review on various additive manufacturing techniques and its implementation in electronic devices, J. Manuf. Syst. 62 (2022) 477–502, https://doi.org/10.1016/j.jmsy.2022.01.002.
[23] Y. Zhang, G. Shi, J. Qin, S.E. Lowe, S. Zhang, H. Zhao, Y.L. Zhong, Recent Progress of Direct Ink Writing of Electronic Components for Advanced Wearable Devices, ACS Appl. Electron. Mater. 1 (9) (2019) 1718–1734, https://doi.org/10.1021/acsaelm.9b00428.
[24] J.A. Lewis, Direct Ink Writing of 3D Functional Materials, Adv. Funct. Mater. 16 (17) (2006) 2193–2204, https://doi.org/10.1002/adfm.200600434.
[25] K. Arapov, A. Goryachev, G. de With, H. Friedrich, A simple and flexible route to large-area conductive transparent graphene thin-films, Synth. Met. 201 (2015) 67–75, https://doi.org/10.1016/j.synthmet.2015.01.016.
[26] K. Arapov, E. Rubingh, R. Abbel, J. Laven, G. de With, H. Friedrich, Conductive screen printing inks by gelation of graphene dispersions, Adv. Funct. Mater. 26 (4) (2016) 586–593, https://doi.org/10.1002/adfm.201504030.
[27] A. Dean, D. Voss, D. Draguljic, Design and Analysis of Experiments, 2nd Edition, Springer, 2017.
[28] G.E. Box, D.W. Behnken, Some new three level designs for the study of quantitative variables, Technometrics 2 (4) (1960) 455–475, https://doi.org/10.1080/00401706.1960.10489912.
[29] NIST/SEMATECH, E-Handbook of statistical methods [online] 2012.
[30] R. Sjoegren, pyDOE2 1.3.0, 2020.
[31] H. 3D, Head Overview, https://hyrel3d.com/wiki/index.php/Head_Overview.
[32] S. Seabold, J. Perktold, Statsmodels: Econometric and Statistical Modeling with Python, in: Python in Science Conference, Austin, Texas, 2010, pp. 92–96.
[33] S. Lamnini, H. Elsayed, Y. Lakhdar, F. Baino, F. Smeacetto, E. Bernardo, Robocasting of advanced ceramics: Ink optimization and protocol to predict the printing parameters - A review, Heliyon 8 (9) (2022) e10651, https://doi.org/10.1016/j.heliyon.2022.e10651.
[34] C.W. Peak, J. Stein, K.A. Gold, A.K. Gaharwar, Nanoengineered colloidal inks for 3D bioprinting, Langmuir 34 (3) (2018) 917–925, https://doi.org/10.1021/acs.langmuir.7b02540.
[35] E.B. Secor, M.H. Dos Santos, S.G. Wallace, N.P. Bradshaw, M.C. Hersam, Tailoring the Porosity and Microstructure of Printed Graphene Electrodes via Polymer Phase Inversion, J. Phys. Chem. C 122 (25) (2018) 13745–13750, https://doi.org/10.1021/acs.jpcc.8b00580.
[36] M. Rebber, M. Trommler, I. Lokteva, S. Ehteram, A. Schropp, S. König, M. Fröba, D. Koziej, Additive-Free, Gelled Nanoinks as a 3D Printing Toolbox for Hierarchically Structured Bulk Aerogels, Adv. Funct. Mater. 32 (19) (2022) 2112914, https://doi.org/10.1002/adfm.202112914.
[37] M.E. Cooke, D.H. Rosenzweig, The rheology of direct and suspended extrusion bioprinting, APL Bioeng. 5 (2021), https://doi.org/10.1063/5.0031475.
[38] L. Li, Z. Deng, M. Chen, Z.-Z. Yu, T.P. Russell, H.-B. Zhang, 3D Printing of Ultralow-Concentration 2D Nanomaterial Inks for Multifunctional Architectures, Nano Lett. 23 (1) (2023) 155–162, https://doi.org/10.1021/acs.nanolett.2c03821.
[39] S.M. Oliveira, L.H. Fasolin, A.A. Vicente, P. Fuciños, L.M. Pastrana, Printability, microstructure, and flow dynamics of phase-separated edible 3D inks, Food Hydrocoll. 109 (2020) 106120, https://doi.org/10.1016/j.foodhyd.2020.106120.
[40] C. O'Mahony, E.U. Haq, C. Silien, S.A. Tofail, Rheological issues in carbon-based inks for additive manufacturing, Micromachines 10 (2) (2019) 99, https://doi.org/10.3390/mi10020099.
[41] L. Liu, Z. Shen, X. Zhang, H. Ma, Highly conductive graphene/carbon black screen printing inks for flexible electronics, J. Colloid Interface Sci. 582 (2021) 12–21, https://doi.org/10.1016/j.jcis.2020.07.106.
[42] S. Jang, A. Boddorff, D.J. Jang, J. Lloyd, K. Wagner, N. Thadhani, B. Brettmann, Effect of material extrusion process parameters on filament geometry and inter-filament voids in as-fabricated high solids loaded polymer composites, Addit. Manuf. 47 (2021) 102313, https://doi.org/10.1016/j.addma.2021.102313.
[43] L. Rizzi, A.F. Wijaya, L.V. Palanisamy, J. Schuster, M. Köhne, S.E. Schulz, Quantifying the influence of graphene film nanostructure on the macroscopic electrical conductivity, Nano Ex. 1 (2) (2020) 020035, https://doi.org/10.1088/2632-959X/abb37a.
[44] C. Fang, J. Zhang, X. Chen, G.J. Weng, Calculating the electrical conductivity of graphene nanoplatelet polymer composites by a Monte Carlo method, Nanomaterials 10 (6) (2020) 1129, https://doi.org/10.3390/nano10061129.
[45] A.G. Kelly, D. O'Suilleabhain, C. Gabbett, J.N. Coleman, The electrical conductivity of solution-processed nanosheet networks, Nat. Rev. Mater. 7 (3) (2022) 217–234, https://doi.org/10.1038/s41578-021-00386-w.
[46] H. Zhang, S.K. Moon, T.H. Ngo, Hybrid Machine Learning Method to Determine the Optimal Operating Process Window in Aerosol Jet 3D Printing, ACS Appl. Mater. Interfaces 11 (19) (2019) 17994–18003, https://doi.org/10.1021/acsami.9b02898.
[47] L.S. Van Hazendonk, C.F. Vonk, W. van Grondelle, N.H. Vonk, H. Friedrich, Data and code related to the manuscript "Towards a predictive understanding of direct ink writing of graphene-based inks", https://doi.org/10.4121/143ec88f-8a41-4d8b-a306-9ff519e4024b, 2023.